AIP | Journal of Applied Physics

Calculation of the piezoelectric and flexoelectric effects in nanowires using a decoupled finite element analysis method

Zhiqiang Zhang, Dalong Geng, and Xudong Wang

Citation: Journal of Applied Physics **119**, 154104 (2016); doi: 10.1063/1.4946843
View online: http://dx.doi.org/10.1063/1.4946843
View Table of Contents: http://scitation.aip.org/content/aip/journal/jap/119/15?ver=pdfcov
Published by the AIP Publishing

Calculation of the piezoelectric and flexoelectric effects in nanowires using a decoupled finite element analysis method

Zhiqiang Zhang,[1,2,a)] Dalong Geng,[2,a)] and Xudong Wang[2,b)]
[1]*School of Power and Mechanical Engineering, Wuhan University, Wuhan, China*
[2]*Department of Materials Science and Engineering, University of Wisconsin-Madison, Madison, Wisconsin 53706, USA*

(Received 15 December 2015; accepted 3 April 2016; published online 20 April 2016)

A simple and effective decoupled finite element analysis method was developed for simulating both the piezoelectric and flexoelectric effects of zinc oxide (ZnO) and barium titanate (BTO) nanowires (NWs). The piezoelectric potential distribution on a ZnO NW was calculated under three deformation conditions (cantilever, three-point, and four-point bending) and compared to the conventional fully coupled method. The discrepancies of the electric potential maximums from these two methods were found very small, validating the accuracy and effectiveness of the decoupled method. Both ZnO and BTO NWs yielded very similar potential distributions. Comparing the potential distributions induced by the piezoelectric and flexoelectric effects, we identified that the middle segment of a four-point bending NW beam is the ideal place for measuring the flexoelectric coefficient, because the uniform parallel plate capacitor-like potential distribution in this region is exclusively induced by the flexoelectric effect. This decoupled method could provide a valuable guideline for experimental measurements of the piezoelectric effects and flexoelectric effects in the nanometer scale. *Published by AIP Publishing*. [http://dx.doi.org/10.1063/1.4946843]

I. INTRODUCTION

Piezoelectricity is a response of electric polarization to a mechanical strain in crystalline dielectrics with noncentrosymmetric crystal structures. Numerous applications of direct and reverse piezoelectric effects play important roles in modern life. In recent years, researchers have constructed comprehensive theoretical frameworks to analyze and predict the piezoelectricity of a broad range of materials.[1–9] Flexoelectricity is a relative new electromechanical coupling phenomenon describing the response of electric polarization to a mechanical strain gradient.[10,11] Unlike piezoelectricity, flexoelectricity appears not only in noncentrosymmetric dielectrics but also in centrosymmetric dielectrics because a strain gradient can break local symmetry.[12,13] Due to its very small effect in bulk materials, flexoelectricity had not attracted much attention since its discovery several decades ago. Strong flexoelectric effects can be introduced by large strain gradients that were found to be feasible in nanoscale materials. Increasing theoretical analysis of the flexoelectric effect in the nanometer regime has been explored recently.[13–16]

Both piezoelectricity and flexoelectricity play a key role in the operation of nanowire (NW)-based nanogenerators (NGs) that convert ambient mechanical energy into electricity.[17–22] NG is a promising technology for charging batteries, powering wearable electronic devices and implantable biomedical devices.[23–31] The working principle of a NW-based NG relies on deforming the NWs to produce electric polarization on the NW surfaces. While the piezoelectric contribution has been intensively studied, little is known about the contribution from the flexoelectricity to the performance of the NGs, only a few papers discussing flexoelectric effect affecting performance of NGs with analytic method[32–35] exist. Numerical analysis of the flexoelectric response in single-crystalline nanowires and understanding the interaction with the piezoelectric effect are one essential step toward effective utilization of the flexoelectric effect in NG design.

Current commercial finite element analysis (FEA) software is capable of calculating piezoelectricity owing to its well-developed theoretical framework. However, the function of solving flexoelectricity is mostly absent. The main approach that most commercial FEA software (e.g., ANSYS, ADINA) use is the fully coupled method, which combines the analyses of both mechanical and electric fields simultaneously.[36] However, this method is not ideal for solving the flexoelectric effects due to the complicity of involving flexoelectric coefficient and strain gradients. Bradley proposed an FEA method for solving the flexoelectricity, but was restrained to 2-dimentional models.[37] In this paper, we developed a decoupled FEA method to calculate the flexoelectric effects of NWs under three different bending conditions. Based on a zinc oxide (ZnO) NW model, the strain-related piezoelectricity was calculated using both our decoupled and conventional fully coupled methods. Very small discrepancies were found between the results of these two methods after only the first calculation cycle, which validated our decoupled method. This decoupled method was further applied to flexoelectricity calculations. The electric potential distributions from both piezoelectric and flexoelectric effects were clearly distinguished for piezoelectric ZnO and

[a)]Z. Zhang and D. Geng contributed equally to this work.
[b)]Email: xudong.wang@wisc.edu

ferroelectric $BaTiO_3$ (BTO) NWs. This calculation provides a guideline for experimentally quantifying the flexoelectric coefficients and designing new NW-based NGs.

II. DECOUPLED FEA METHOD

To simplify the derivation, we assume that the NW bending is very small,[38] so that the electromechanical properties of piezoelectric materials can be described by the constitutive equations

$$\sigma_{ij} = c_{ijkl}\varepsilon_{kl} - e_{kij}E_k, \tag{1}$$

$$D_i = e_{ikl}\varepsilon_{kl} + k_{ik}E_k = P_i + k_{ik}E_k, \tag{2}$$

where σ, c, ε, e, E, D, P, and k are the mechanical stress tensor, the mechanical stiffness tensor, the mechanical strain tensor, the piezoelectric coefficient matrix, the electric field, the electric displacement, the electric polarization, and the dielectric constant, respectively. The constitutive equations of flexoelectricity have similar forms except strain and electric field being replaced by strain gradient and electric field gradient. Both piezoelectric and flexoelectric effects exist in a strained non-centrosymmetric material. Therefore, the constitutive equations should describe these two effects together.[39,40] In order to easily compare the results from the two effects, here we discuss the two effects separately. The piezoelectric coefficient, a third-rank tensor e_{kij} is changed to the flexoelectric coefficient μ_{ijkl}, a fourth-rank tensor as well

$$\sigma_{ij} = c_{ijkl}\varepsilon_{kl} - \mu_{ijkl}E_{k,j}, \tag{3}$$

$$D_i = \mu_{ijkl}\varepsilon_{jk,l} + k_{ik}E_k = P_i + k_{ik}E_k, \tag{4}$$

where the complete expansion of the strain gradient $\varepsilon_{jk,l}$ and the direct flexoelectric coefficient matrix μ_{ijkl} can be found in supplementary material S2.[46]

The decoupled FEA method was developed to take into account strain gradient and electric field gradient in addition to the strain and electric fields for calculating the electric potential distribution. Unlike the fully coupled method detailed in supplementary material S1,[46] the decoupled method deals with the displacement field and the electric field separately. When the displacement field is considered, only the displacement vector $\{u_i\}$ exists at the node in each element. When we calculate the electric field, the only degree of freedom is electric potential $\{\phi_i\}$. These two processes are described in Equations (5) and (6), respectively,

$$[K_{uu}]\{u_i\} = \{F_B\} + \{F_S\} + \{F_P\}, \tag{5}$$

$$[K_{\emptyset\emptyset}]\{\emptyset_i\} = \{Q_B\} + \{Q_S\} + \{Q_P\}, \tag{6}$$

where $[K_{uu}]$ and $[K_{\phi\phi}]$ are stiffness matrix and dielectric matrix, respectively. $\{F_B\}$, $\{F_S\}$, and $\{F_P\}$ are body force vector, surface force vector, and concentrated force vector, respectively; $\{Q_B\}$, $\{Q_S\}$, and $\{Q_P\}$ are body charge vector, surface charge vector, and point charge vector, respectively. By doing so, we can solve the displacement field first to obtain the strain or strain gradient and then calculate the electric polarization induced by the strain or strain gradient. In a complete cycle of the decoupled method, $\{Q_B\}$ and $\{Q_S\}$ were substituted in Eq. (6) to obtain $\{\phi_i\}$ and then the electric field and electric field gradient, which will be used to calculate the stress based on the constitutive questions of piezoelectric and flexoelectric effects (Eqs. (1) and (3)). The stress was presented by $\{F_B\}$ and $\{F_S\}$ to calculate $\{u_i\}$. This process can be repeated until a satisfactory result is reached.

III. APPLICATION OF THE DECOUPLED FEA METHOD FOR PIEZOELECTRIC POTENTIAL CALCULATION

The decoupled FEA method was first applied to the calculation of the piezoelectric effects.[41] Here, the constitutive equations of the piezoelectric effects become[42]

$$\{\sigma\}^{(0)} = [c^E]\{\varepsilon\}^{(0)}, \tag{7}$$

$$\{D\}^{(1)} = [e]\{\varepsilon\}^{(0)} + [\chi]\{E\}^{(1)}. \tag{8}$$

Eq. (7) describes the relation between strain and stress without the converse piezoelectric effect. Eq. (8) describes the direct piezoelectric effect. The number in superscripts represents the number of calculation iteration. Here, a piezoelectric ZnO NW is used as a model system due to its well-known mechanical and piezoelectric properties. The piezoelectric potential distribution generated by three bending situations (cantilever, three point, and four point bending) is calculated and compared to the conventional fully coupled method.

Cantilever bending is the most common deformation scenario for NWs in NG applications. Based on the Saint-Venant theory of bending, the mechanical strain is given by[34,43]

$$\{\varepsilon\}^{(0)} = \begin{Bmatrix} \frac{\nu f_y}{EI_{xx}} y(l-z) \\ \frac{\nu f_y}{EI_{xx}} y(l-z) \\ -\frac{f_y}{EI_{xx}} y(l-z) \\ \frac{f_y}{I_{xx}} \frac{3+2\nu}{4E}\left[a^2 - y^2 - \frac{1-2\nu}{3+2\nu}x^2\right] \\ -\frac{f_y}{I_{xx}} \frac{1+2\nu}{2E} xy \\ 0 \end{Bmatrix}. \tag{9}$$

This strain matrix can be directly used to calculate the electric polarization ($\vec{P}^R$) following Eq. (8):

$$\vec{P}^R = [e]\{\varepsilon\}^{(0)} = \begin{Bmatrix} -\frac{f_y}{EI_{xx}}\left(\frac{1}{2}+\nu\right)e_{15}xy \\ \frac{f_y}{EI_{xx}}\left(\frac{3}{4}+\frac{\nu}{2}\right)e_{15}\left(a^2 - y^2 - \frac{1-2\nu}{3+2\nu}x^2\right) \\ \frac{f_y}{EI_{xx}}(2\nu e_{31} - e_{33})y(l-z) \end{Bmatrix}. \tag{10}$$

By assuming no free charges in the nanowire and according to Gauss's law, the body charge density can be defined as

$$\rho^R = -\nabla \cdot \vec{P}^R = \frac{f_y}{EI_{xx}}[2(1+\nu)e_{15} + 2\nu e_{31} - e_{33}]y, \quad (11)$$

and the surface charge density as

$$\Sigma^R = -\vec{n} \cdot (0 - \vec{P}^R) = \vec{n} \cdot \vec{P}^R. \quad (12)$$

Therefore, this case can be considered as an electrostatic problem, and the body charge density and the surface charge density can represent the electric polarization as boundary conditions in the FEA model to calculate the piezoelectric potential.

The piezoelectric potential distribution along a ZnO NW (600 nm long, 25 nm in radius, and under a force of 80 nN on the free end) was calculated using the decoupled FEA method (material parameters used in the calculation were listed in supplementary material S3[46]). Figure 1(a) schematically shows the electric dipole distribution inside the ZnO NW when the force f_y is applied on the left end. Only body charge exists in this case. The calculated potential distribution is plotted in a 3D NW geometry, revealing a parallel plate capacitor-like behavior (Figure 1(b)). Charges on both ends of the NW have negligible effect on the electric field of the entire NW due to the significantly small diameter compared to the NW's length. In order to validate the accuracy of the decoupled method, the piezoelectric response of the same NW was also calculated using the fully coupled method (supplementary material S1[46]). The potential distributions along the axial cross section calculated by both methods are shown in Figures 1(c) and 1(d), respectively. These two methods yielded very similar potential distributions. The difference between the maximum electric potential values from the two methods was found to be 6% (0.265 V from the decouple method versus 0.282 V from the fully coupled method).

The same ZnO NW model (600 nm in length and 25 nm in radius) was then analyzed under the three-point bending situation. An external force f_y of 80 nN was assumed to be applied at the middle of the NW. According to the classic mechanics, the maximum bending strain appears at the middle point that is bearing the external force. The shear strain exhibits a mirror distribution versus the center plane of the NW. Thus, the strains of the left part $\{\varepsilon\}_l$ and the right part $\{\varepsilon\}_r$ of the ZnO NW can be expressed by Eqs. (13) and (14), respectively,

$$\{\varepsilon\}_l = \begin{Bmatrix} \frac{\nu f_y}{2EI_{xx}} yz \\ \frac{\nu f_y}{2EI_{xx}} yz \\ -\frac{f_y}{2EI_{xx}} yz \\ -\frac{f_y}{2I_{xx}} \frac{3+2\nu}{4E}\left[a^2 - y^2 - \frac{1-2\nu}{3+2\nu}x^2\right] \\ \frac{f_y}{2I_{xx}} \frac{1+2\nu}{2E} xy \\ 0 \end{Bmatrix}, \quad (13)$$

$$\{\varepsilon\}_r = \begin{Bmatrix} \frac{\nu f_y}{2EI_{xx}} y(l-z) \\ \frac{\nu f_y}{2EI_{xx}} y(l-z) \\ -\frac{f_y}{2EI_{xx}} y(l-z) \\ \frac{f_y}{2I_{xx}} \frac{3+2\nu}{4E}\left[a^2 - y^2 - \frac{1-2\nu}{3+2\nu}x^2\right] \\ -\frac{f_y}{2I_{xx}} \frac{1+2\nu}{2E} xy \\ 0 \end{Bmatrix}. \quad (14)$$

The body charge density of the left part and the right part can be written as follows:

$$\rho_r^R = -\rho_l^R = \frac{f_y}{2EI_{xx}}[2(1+\nu)e_{15} + 2\nu e_{31} - e_{33}]y. \quad (15)$$

The surface charge density of the NW surface remains neutral

$$\sum_l^R = \sum_r^R = 0. \quad (16)$$

The charge distribution can be represented by the electric dipoles inside the NW under the three-point bending condition (Figure 1(e)), and the corresponding electric potential distribution is shown in Figure 1(f). The electric potential distribution in each half of the NW is very much similar to that of a parallel plate capacitor (or the cantilever beam case). However, the signs of the electric potential in the two sides are opposite. This symmetric distribution can be considered as if two cantilever beams were joined together head-to-head. The opposite potential sign is a result of the opposite polarization directions ([0001] versus [000–1] of the ZnO NW case) of these two cantilever beams. The electric potential is zero at the center point where the external force is applied because the induced body charges are neutralized at the middle. The axial cross-sectional plots of the decoupled and coupled methods (Figures 1(g) and 1(h), respectively) clearly reveal that both methods can yield the same results. The discrepancy of the maximum electric potential between these two methods was only 0.6% (0.133 V from the decouple method versus 0.134 V from the fully coupled method).

The same ZnO NW model was further used to analyze the four-point bending case. Two external forces of the same value, 40 nN, were exerted at the two points 150 nm away from both ends. Under this bending situation, the middle segment between the two bearing points exhibits no shear strain but only bending strain, while the two end segments of the beam have opposite shear strain. The strain function in the left, middle, and right segments of the ZnO NW is presented as $\{\varepsilon\}_l$, $\{\varepsilon\}_m$, and $\{\varepsilon\}_r$, respective in the following equations:

$$\{\varepsilon\}_l = \begin{Bmatrix} \frac{\nu f_y}{EI_{xx}} yz \\ \frac{\nu f_y}{EI_{xx}} yz \\ -\frac{f_y}{EI_{xx}} yz \\ -\frac{f_y}{I_{xx}} \frac{3+2\nu}{4E} \left[a^2 - y^2 - \frac{1-2\nu}{3+2\nu} x^2 \right] \\ \frac{f_y}{I_{xx}} \frac{1+2\nu}{2E} xy \\ 0 \end{Bmatrix}, \quad (17)$$

$$\{\varepsilon\}_m = \begin{Bmatrix} \frac{\nu f_y l}{4EI_{xx}} y \\ \frac{\nu f_y l}{4EI_{xx}} y \\ -\frac{f_y l}{4EI_{xx}} y \\ 0 \\ 0 \\ 0 \end{Bmatrix}, \quad (18)$$

$$\{\varepsilon\}_r = \begin{Bmatrix} \frac{\nu f_y}{EI_{xx}} y(l-z) \\ \frac{\nu f_y}{EI_{xx}} y(l-z) \\ -\frac{f_y}{EI_{xx}} y(l-z) \\ \frac{f_y}{I_{xx}} \frac{3+2\nu}{4E} \left[a^2 - y^2 - \frac{1-2\nu}{3+2\nu} x^2 \right] \\ -\frac{f_y}{I_{xx}} \frac{1+2\nu}{2E} xy \\ 0 \end{Bmatrix}. \quad (19)$$

According to the decoupled FEA method, the body charge densities of the left and the right segments follow the same relations described in Eq. (15), whereas the body charge density of the middle segment is zero. Similar to the three point bending case, the surface charge densities of the left, middle, and right segments are all zero.

The schematic diagram of the electric dipole distribution under the four-point bending condition is shown in Figure 1(i). The 3D electric potential distribution calculated by the decoupled method is illustrated in Figure 1(j). Since there is no body charge induced in the middle segment, no piezoelectric potential is generated there. The parallel plate capacitor-type

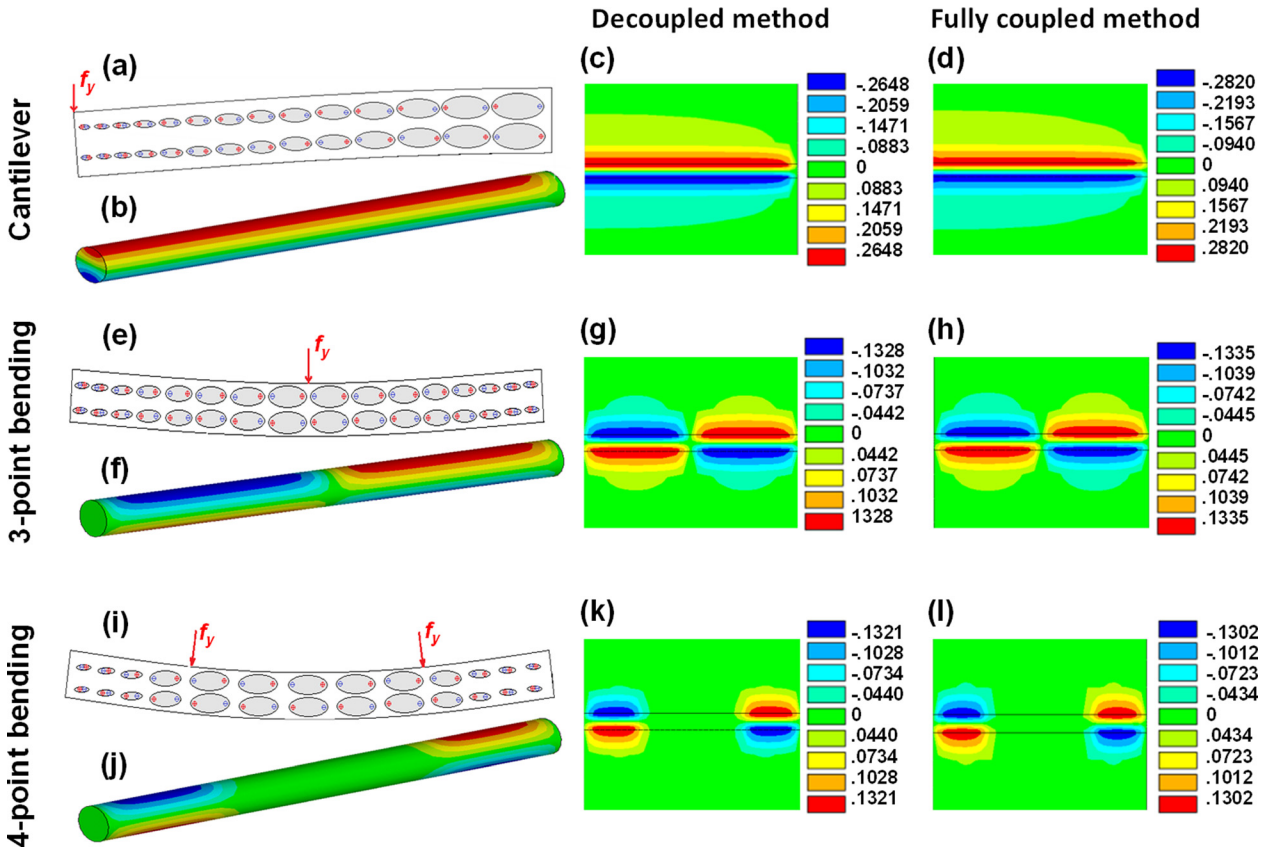

FIG. 1. Calculated piezoelectric potential distribution along a ZnO. Study case of a cantilever bending mode (a)–(d), a 3-point bending mode (e)–(h), and a 4-point bending mode (i)–(l). (a), (e), and (i) Schematic electric dipole distributions along a ZnO NW beam. (b), (f), and (j) 3D piezoelectric potential distributions along a ZnO NW beam calculated by the decoupled method. (c), (g), and (k) The potential distributions along the axial cross section calculated by the decoupled method. (d), (h), and (l) The potential distributions along the axial cross section calculated by the fully coupled method.

potential distribution is produced on both end segments with opposite signs. This type of potential distribution can be considered similar to the case of three-point bending with an extended central neutral potential zone. Comparing the axial cross-sectional region from the decoupled FEA method (Figure 1(k)) and the fully coupled FEA method (Figure 1(l)) also revealed the same potential distribution with a discrepancy of electric potential maximum as small as 1.5% (0.132 V from the decouple method versus 0.130 V from the fully coupled method).

By comparing the potential distribution and the potential maximum discrepancy between our decoupled and conventional fully coupled methods, we can conclude that the decoupled FEA method is a fairly simple and an efficient approach to predict the electric potential distribution induced by the piezoelectric effects.

It should be noted that in wurtzite material systems, the second order piezoelectric effect, i.e., the nonlinear piezoelectric component, has a profound influence on the overall piezoelectric polarization.[44,45] However, the fully coupled FEA method cannot be used directly to calculate the nonlinear effect either. Based on the established theoretical framework,[45] the second order piezoelectric effect of the ZnO NW was also calculated by the decoupled FEA method under the cantilever, three-point bending, and four-point bending conditions (supplementary material S4[46]). From the results, the nonlinear piezoelectric effect can make a significant contribution to the overall potential, especially for the cantilever's case under larger strain.

IV. APPLICATION OF THE DECOUPLED FEA METHOD FOR FLEXOELECTRIC POTENTIAL CALCULATION

After validating the decoupled FEA method in calculating the piezoelectric response, it was then used to calculate the flexoelectric effect, where the strain gradient and the electric field gradient become the essential components. The complete expansions of the strain gradient and the flexoelectric coefficient are included in supplementary material S2.[46] To be consistent with other calculations reported previously,[32,43] we also assume that both ZnO and BTO are isotropic. By applying the decoupled FEA method, the constitutive equations of the flexoelectric effects become

$$\{\sigma\}^{(0)} = [c^E]\{\varepsilon\}^{(0)}, \tag{20}$$

$$\{D\}^{(1)} = [\mu]\left\{\frac{\partial \varepsilon}{\partial x_l}\right\}^{(0)} + [\chi]\{E\}^{(1)}. \tag{21}$$

Here, we only consider mechanical strain in Eq. (20) and the polarization solely induced by pure mechanical strain gradient in Eq. (21). Only one calculation cycle was applied in the FEA process as we did in the piezoelectric effects' case to simplify the calculation. The same ZnO NW model was used under the three different bending conditions for flexoelectricity calculation.

In a cantilever beam mode, applying Eq. (9) of the Saint-Venant theory of bending, Eqs. (S9) and (S10) in supplementary material S2,[46] to the constitutive equations yielded the polarization induced by the flexoelectric effect

$$\vec{P}^R = [\mu]\left\{\frac{\partial \varepsilon}{\partial x_l}\right\}^{(0)} = \begin{Bmatrix} P_x \\ P_y \\ P_z \end{Bmatrix}, \tag{22}$$

where $P_x = \mu_{11}\varepsilon_{111} + \mu_{14}\varepsilon_{221} + \mu_{14}\varepsilon_{331} + 2\mu_{111}\varepsilon_{133} + 2\mu_{111}\varepsilon_{122} = 0$, $P_y = \mu_{14}\varepsilon_{112} + \mu_{11}\varepsilon_{222} + \mu_{14}\varepsilon_{332} + 2\mu_{111}\varepsilon_{233} + 2\mu_{111}\varepsilon_{121} = \frac{f_y}{EI_{xx}}(l-z)(\mu_{14}\nu + \mu_{11}\nu - \mu_{14})$, and $P_z = \mu_{14}\varepsilon_{113} + \mu_{14}\varepsilon_{223} + \mu_{11}\varepsilon_{333} + 2\mu_{111}\varepsilon_{232} + 2\mu_{111}\varepsilon_{131} = \frac{f_y}{EI_{xx}}y[-2\mu_{14}\nu + \mu_{11} - 2\mu_{111}(1+\nu)]$.

Similarly, we define the body charge density by

$$\rho^R = -\nabla \cdot \vec{P}^R = 0, \tag{23}$$

and the surface charge density by

$$\sum{}^R = -\vec{n} \cdot (0 - \vec{P}^R) = \vec{n} \cdot \vec{P}^R. \tag{24}$$

The body charge density and the surface charge density were used as the boundary conditions in the FEA calculation. Different from the piezoelectric responses, the flexoelectric polarization is produced only by the surface charge, and the body charge density becomes zero. The surface charge density on both end surfaces was ignored because it would not induce an appreciable intrinsic electric field inside the NW due to the NW's large aspect ratio. The surface charge density on the cylindrical surface is given by

$$\begin{aligned}\sum_{r=a}^{R} &= \frac{f_y}{EI_{xx}}(L-z)(\mu_{14}\nu + \mu_{11}\nu - \mu_{14})\sin(\theta) \\ &= \frac{f_y}{EI_{xx}}(L-z)\mu_e \sin(\theta).\end{aligned} \tag{25}$$

Here, θ is the polar angle in the radial cross section of the NW (Figure 2(a)). The electric potential maxima appear at the middle of the top surface ($\theta = 90°$) and the middle of the bottom surface ($\theta = 270°$). The dipole distribution inside the NW in response to the flexoelectric effect is schematically shown in Figure 2(b-i). The dipoles inside the NW line perpendicularly to the NW's axis so that the body charge is cancelled and only surface charge exists.

For the convenience of calculation, we define an equivalent flexoelectric parameter

$$\mu_e = \mu_{14}\nu + \mu_{11}\nu - \mu_{14}. \tag{26}$$

By assuming the external force at the free end is 80nN and $\mu_e = -1$nC/m, the electric potential distribution as a result of the flexoelectric effect was calculated, and the 3D plot is shown in Figure 2(b-ii). The right-hand-side is the fixed end of the NW. The top surface of the NW is positively charged, and the bottom surface is negatively charged. The electric potential is at maximum immediately next to the fixed end and decreases gradually towards the free end, which can be clearly observed from the axial cross-sectional image (Figure 2(b-iii)). The radial cross-sectional potential profile at the maximum potential region is shown on the top-right inset of Figure 2(b-iii). The nonuniform electric potential distribution is correlated to the strain gradient in the deflected NW cantilever

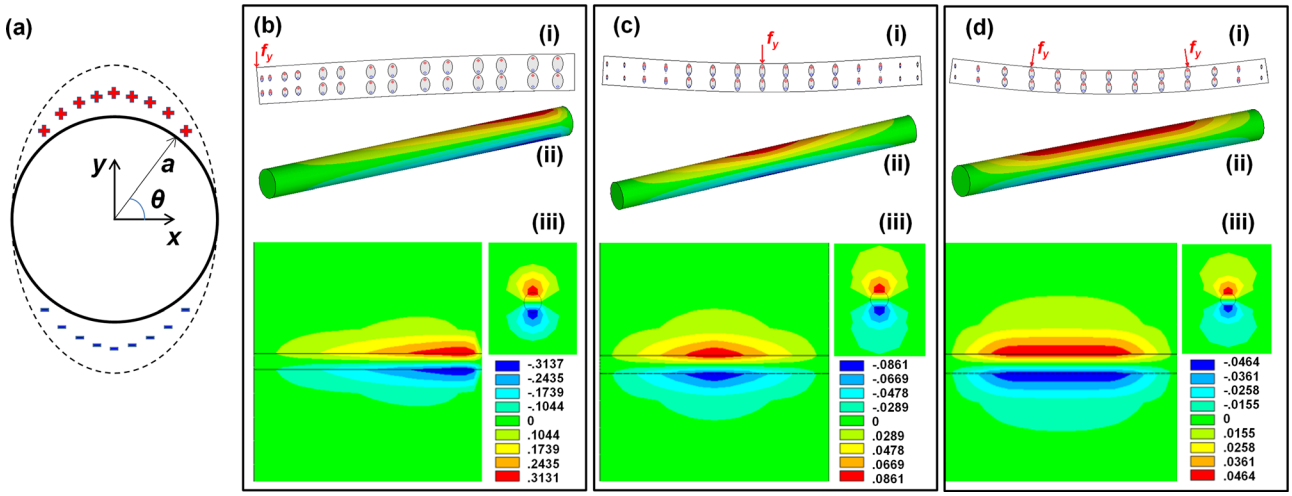

FIG. 2. (a) Schematic of the surface charge distribution on the radial cross-section of a cylindrical NW. (b) Flexoelectric effect-induced polarization in a cantilever mode. (c) Flexoelectric effect-induced polarization in a 3-point bending mode. (d) Flexoelectric effect-induced polarization in a 4-point bending mode. In (b)–(d), (i) schematic electric dipole distribution; (ii) 3D potential distributions along a ZnO NW beam; and (iii) the potential distributions along the axial cross section. The top-right inset is the radial cross-sectional potential profile at the maximum potential region.

beam, where the maximum of the strain gradient occurs at the fixed point. Strained ZnO structures have both piezoelectric and flexoelectric effects. Reference 32 provided an analytic result of electric potential distribution in ZnO considering both effects at the same time. In order to validate our decoupled method, an identical set of parameters were used in our calculation, and the results matched very well to those reported in Ref. 32 (see supplementary material S5[46]).

When the ZnO NW is under the three-point bending condition, the dipole distribution induced by the flexoelectric effect is schematically shown in Figure 2(c-i). Based on the strain formula (13) and (14), the surface charge density of the NW surface is given by

$$\sum_{r=a}^{R} = \frac{f_y}{EI_{xx}} z\mu_e \sin(\theta),\ (0 < z < l/2), \tag{27}$$

$$\sum_{r=a}^{R} = \frac{f_y}{EI_{xx}} (l-z)\mu_e \sin(\theta),\ (l/2 < z < l). \tag{28}$$

When an external force of 80 nN is exerted at the center point of the ZnO NW, the flexoelectric effect-generated electric potential distribution is shown in Figure 2(c-ii). Opposite to the piezoelectric case, the maximum potential is located at the center force-bearing point. The potential decreases symmetrically towards both ends and reaches the zero point, as illustrated by the axial cross-sectional potential profile in Figure 2(c-iii). This potential distribution is in accordance with the strain gradient distribution in the three-point bending condition, where the maximum strain gradient is located at the center force-bearing point. The right inset of Figure 2(c-iii) shows the radial cross-sectional potential profile at the center point, revealing the maximum potential that can be produced by the flexoelectric effect.

A similar procedure was then applied to calculate the flexoelectric effect of the ZnO NW in a four-point bending case, where two external forces of 40 nN each were applied to the $l/4$ and $3\,l/4$ points on the NW beam. The corresponding dipole distribution is schematically shown in Figure 2(d-i). From strain formula in Eqs. (17)–(19), the electric polarization can be obtained from the strain gradient, and the surface charge density on the NW surface is given by

$$\sum_{r=a}^{R} = \frac{f_y}{EI_{xx}} z\mu_e \sin(\theta),\ \left(0 < z < \frac{l}{4}\right), \tag{29}$$

$$\sum_{r=a}^{R} = \frac{f_y}{EI_{xx}} (l-z)\mu_e \sin(\theta),\ \left(\frac{3l}{4} < z < l\right), \tag{30}$$

$$\sum_{r=a}^{R} = \frac{f_y l}{4EI_{xx}} \mu_e \sin(\theta),\ \left(\frac{l}{4} < z < \frac{3l}{4}\right). \tag{31}$$

As shown by the 3D plot (Figure 2(d-ii)) and axial cross-section (Figure 2(d-iii)) of the electric potential distribution, the uniform bending segment (center segment) exhibits a parallel plate capacitor-type electric potential profile with the maximum value at the top and bottom surfaces. This is well coordinated with the maximum and uniform strain gradient between the two force bearing points. In the left and right segments, the electric potential drops rapidly to zero toward both ends, similar to the three-point bending case. Recall the piezoelectric case, the center segment exhibits no electric potential. The large and uniform potential in the center segment is purely the result of the flexoelectric effect, which offers an ideal scenario for characterizing the flexoelectric effect.

V. APPLICATION OF THE DECOUPLED FEA METHOD TO CALCULATING $BaTiO_3$ NWs

$BaTiO_3$ (BTO) is a ferroelectric material and has different crystal structures and piezoelectric/flexoelectric properties compared to ZnO. The decoupled FEA method will be further applied to BTO NWs to calculate the piezoelectric

and flexoelectric responses under the three different bending conditions. According to the crystal structure (perovskite), the cross section of a $BaTiO_3$ (BTO) NW is defined as a square. The size of the BTO NW used in our simulation is defined as 300 nm in length and 10 nm in width, and the external force is assumed to be 80 nN.

The piezoelectric potential distributions were calculated based on the rectangular BTO NW under the cantilever, three-point, and four-point bending conditions, respectively. The strain of a BTO NW cantilever and the electric polarization induced by the piezoelectric effect are given by the following relations:

$$\{\varepsilon\}^{(0)} = \begin{Bmatrix} \frac{\nu f_y}{EI_{xx}} y(l-z) \\ \frac{\nu f_y}{EI_{xx}} y(l-z) \\ -\frac{f_y}{EI_{xx}} y(l-z) \\ \frac{f_y(1+\nu)}{EI_{xx}}\left(y^2 - \frac{1}{4}b^2\right)\left[5nx^4 + 3\left(m - \frac{1}{4}b^2 n\right)x^2 - \frac{1}{4}b^2 m - 1\right] \\ -\frac{2f_y(1+\nu)}{EI_{xx}} y\left[nx^5 + \left(m - \frac{1}{4}b^2 n\right)x^3 - \frac{1}{4}b^2 mx\right] \\ 0 \end{Bmatrix}, \tag{32}$$

$$\vec{P}^R = [e]\{\varepsilon\}^{(0)} = \begin{bmatrix} -\frac{2f_y(1+\nu)}{EI_{xx}} e_{15}\left[nx^5 + \left(m - \frac{1}{4}b^2 n\right)x^3 - \frac{1}{4}b^2 mx\right] \\ \frac{f_y(1+\nu)}{EI_{xx}} e_{15}\left(y^2 - \frac{1}{4}b^2\right)\left[5nx^4 + 3\left(m - \frac{1}{4}b^2 n\right)x^2 - \frac{1}{4}b^2 m - 1\right] \\ \frac{f_y}{EI_{xx}}(2\nu e_{31} - e_{33}) y(l-z) \end{bmatrix}. \tag{33}$$

The body charge density can be calculated following Eq. (11) in the ZnO NW case. As for the three-point and four-point bending cases, the same corresponding equations in the ZnO NW case can also be directly applied. As shown in Figures 3(a)–3(c), the calculated electric potential distributions are very similar to those calculated from the ZnO NWs, and the parallel plate capacitor-like behavior was obtained as a result of the piezoelectric effect. In addition, to compare these two methods, the results of the piezoelectric effect of BTO NW under the three different bending conditions were calculated using the two methods (supplementary material S6[46]). The results from the two methods matched very well, suggesting our decoupled method is indeed simple and effective.

For potential calculation induced by the flexoelectric effect, the same process was then applied to calculate the potential distribution in the BTO NW. In the cantilever mode, Eq. (22) is used to calculate the electric polarization, and the surface charge density can thus be given as

$$\sum_{y=\pm b/2}^{R} = \pm \frac{f_y}{EI_{xx}}(l-z)\mu_e. \tag{34}$$

Under the three-point bending condition, the flexoelectric effect-induced surface charge density along the BTO NW can be given in two halves as

$$\sum_{y=\pm b/2}^{R} = \pm \frac{f_y}{EI_{xx}} z\mu_e, \ (0 < z < l/2), \tag{35}$$

$$\sum_{y=\pm b/2}^{R} = \pm \frac{f_y}{EI_{xx}}(l-z)\mu_e, \ (l/2 < z < l). \tag{36}$$

For the four-point bending condition, the surface charge density is given in three segments where the BTO NW exhibits gradient and uniform strains

$$\sum_{y=\pm b/2}^{R} = \pm \frac{f_y}{EI_{xx}} z\mu_e, \ \left(0 < z < \frac{l}{4}\right), \tag{37}$$

$$\sum_{y=\pm b/2}^{R} = \pm \frac{f_y l}{4EI_{xx}}\mu_e, \ \left(\frac{l}{4} < z < \frac{3l}{4}\right), \tag{38}$$

$$\sum_{y=\pm b/2}^{R} = \pm \frac{f_y}{EI_{xx}}(l-z)\mu_e, \ \left(\frac{3l}{4} < z < l\right). \tag{39}$$

The corresponding calculated electric potential distributions are shown in Figures 3(d)–3(f) for the cantilever, three-point, and four-point bending conditions, respectively. The constants used in our calculation are included in supplementary material S3.[46] It can be clearly seen that the BTO NW exhibits similar potential distribution as those calculated from the

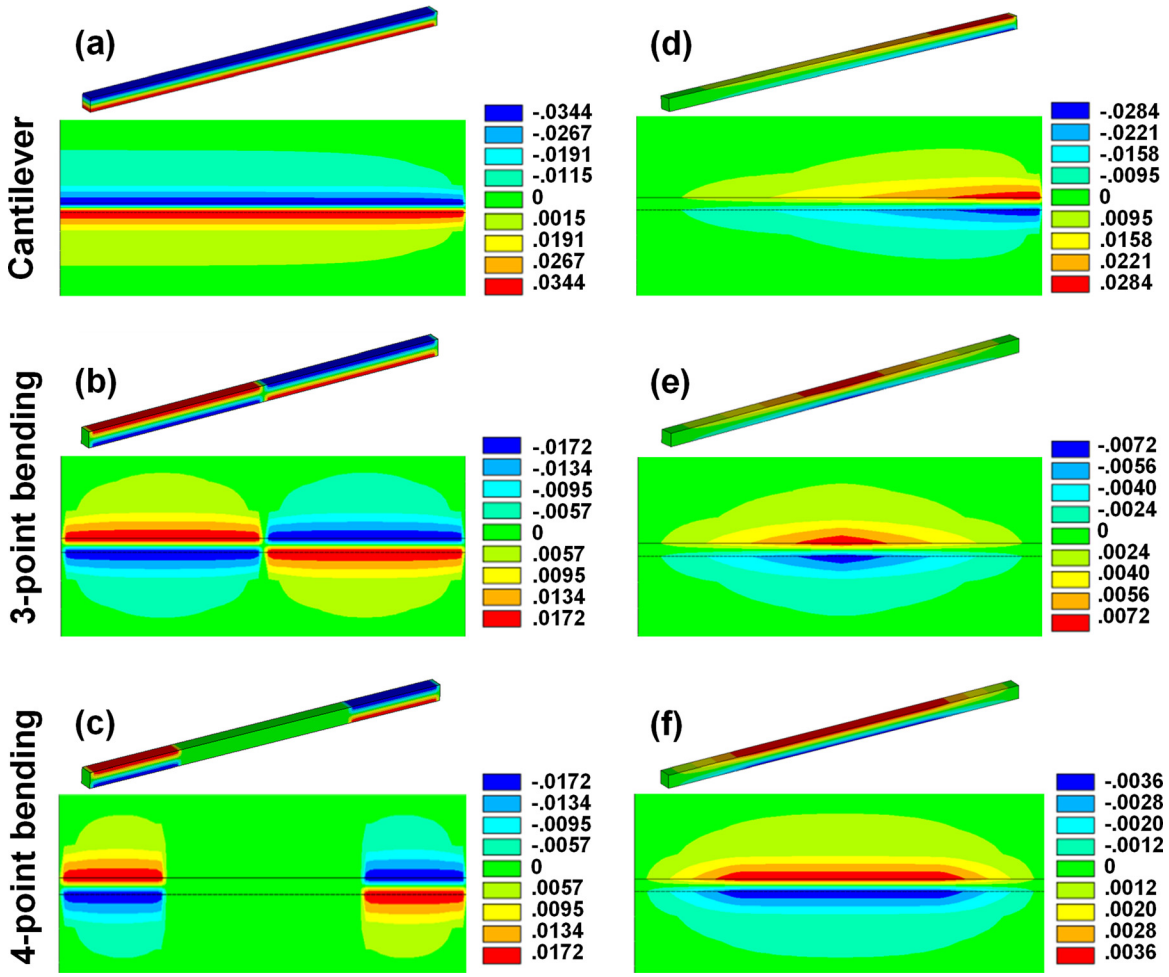

FIG. 3. Piezoelectric (a)–(c) and flexoelectric (d)–(f) potential distributions along a BTO NW beam calculated by the decoupled method. (a) and (d) Study case of a cantilever bending mode. (b) and (e) Study case of a 3-point bending case. (c) and (f) Study case of a 4-point bending case.

ZnO NW in all three cases. For the rectangular geometry, the potential maximum is more uniformly distributed on the top and bottom flat surfaces, instead of a gradual distribution on the cylindrical surfaces. This geometry could therefore provide more accurate measurement of the flexoelectric coefficient compared to cylindrical beams.

VI. CONCLUSION

In summary, we developed a simple and effective decoupled FEA method to calculate the piezoelectric and flexoelectric effects in NW beams. In the decoupled FEA method, the displacement field and the electric field were considered separately. By substituting the strain or strain gradient into the constitutive equations, the electric polarization could be solved exclusively by the mechanical deformation. Following the Gauss's law, the body charge density and the surface charge density were defined separately and were used as the boundary conditions for FEA calculation of the electric potential distribution in a bent NW. The FEA results from our decoupled method were compared to the conventional fully coupled methods based on a ZnO NW under the three deformation conditions: cantilever, three-point, and four-point bending. The discrepancies of the electric potential maximum between these two methods were found very close to each other with just one calculation cycle, showing that our decoupled method can accurately and effectively calculate the strain-induced polarization in a much simpler way. The electric potential induced by the piezoelectric and flexoelectric effects was calculated separately on both ZnO and BTO NW modes, and the distinct potential distributions were obtained between these two effects. Significantly, a uniform parallel plate capacitor-like potential distribution could be generated by the flexoelectric effect in the middle uniformly strained segment under the four-point bending condition, where the piezoelectric effect had zero effect to the potential. This discovery suggested that the middle region of a four-point bending NW is an ideal situation for determining the flexoelectric effect, particularly for a rectangular-shaped NW. The decoupled method can provide a valuable numerical guideline for experimental measurements of the piezoelectric and flexoelectric effects in the nanometer scale.

ACKNOWLEDGMENTS

We acknowledge support of the National Science Foundation (NSF) under Award No. CMMI-1148919. Z.Z. is thankful for the support of China Scholarship Council (CSC).

[1]A. Beya-Wakata, P. Y. Prodhomme, and G. Bester, Phys. Rev. B **84**, 195207 (2011).
[2]Y. F. Duan, G. Tang, C. Q. Chen, T. J. Lu, and Z. G. Wu, Phys. Rev. B **85**, 054108 (2012).
[3]A. Erba, K. E. El-Kelany, M. Ferrero, I. Baraille, and M. Rerat, Phys. Rev. B **88**, 035102 (2013).
[4]A. Roy, M. Stengel, and D. Vanderbilt, Phys. Rev. B **81**, 014102 (2010).
[5]G. Saghi-Szabo, R. E. Cohen, and H. Krakauer, Phys. Rev. B **59**, 12771 (1999).
[6]N. Sai and E. J. Mele, Phys. Rev. B **68**, 241405 (2003).
[7]C. W. Swartz and X. F. Wu, Phys. Rev. B **85**, 054102 (2012).
[8]Z. C. Tu and X. Hu, Phys. Rev. B **74**, 035434 (2006).
[9]Z. G. Wu and H. Krakauer, Phys. Rev. B **68**, 014112 (2003).
[10]V. L. Indenbom, E. B. Loginov, and M. A. Osipov, Kristallografiya **26**, 1157 (1981).
[11]A. K. Tagantsev, Phys. Rev. B **34**, 5883 (1986).
[12]P. Zubko, G. Catalan, A. Buckley, P. R. L. Welche, and J. F. Scott, Phys. Rev. Lett. **99**, 167601 (2007).
[13]M. S. Majdoub, P. Sharma, and T. Cagin, Phys. Rev. B **77**, 125424 (2008).
[14]G. Catalan, B. Noheda, J. McAneney, L. J. Sinnamon, and J. M. Gregg, Phys. Rev. B **72**, 020102 (2005).
[15]S. V. Kalinin and V. Meunier, Phys. Rev. B **77**, 033403 (2008).
[16]M. S. Majdoub, R. Maranganti, and P. Sharma, Phys. Rev. B **79**, 115412 (2009).
[17]B. Kumar and S. W. Kim, Nano Energy **1**, 342 (2012).
[18]Y. Qin, X. Wang, and Z. L. Wang, Nature **457**, 340 (2009).
[19]X. D. Wang, Nano Energy **1**, 13 (2012).
[20]X. D. Wang, Y. F. Gao, Y. G. Wei, and Z. L. Wang, Nano Res. **2**, 177 (2009).
[21]X. D. Wang, J. H. Song, J. Liu, and Z. L. Wang, Science **316**, 102 (2007).
[22]Z. L. Wang and J. H. Song, Science **312**, 242 (2006).
[23]A. P. Chandrakasan, N. Verma, and D. C. Daly, Annu. Rev. Biomed. Eng. **10**, 247 (2008).
[24]J. M. Donelan, Q. Li, V. Naing, J. A. Hoffer, D. J. Weber, and A. D. Kuo, Science **319**, 807 (2008).
[25]J. Granstrom, J. Feenstra, H. A. Sodano, and K. Farinholt, Smart Mater. Struct. **16**, 1810 (2007).
[26]G. K. Ottman, H. F. Hofmann, A. C. Bhatt, and G. A. Lesieutre, IEEE Trans. Power Electron. **17**, 669 (2002).
[27]J. A. Paradiso and T. Starner, IEEE Pervasive Comput. **4**, 18 (2005).
[28]S. Priya, J. Electroceram. **19**, 167 (2007).
[29]C. Xu, C. F. Pan, Y. Liu, and Z. L. Wang, Nano Energy **1**, 259 (2012).
[30]R. Yang, Y. Qin, C. Li, G. Zhu, and Z. L. Wang, Nano Lett. **9**, 1201 (2009).
[31]H. L. Zhang, Y. Yang, T. C. Hou, Y. J. Su, C. G. Hu, and Z. L. Wang, Nano Energy **2**, 1019 (2013).
[32]Q. Deng, M. Kammoun, A. Erturk, and P. Sharma, Int. J. Solids Struct. **51**, 3218 (2014).
[33]X. Jiang, W. Huang, and S. Zhang, Nano Energy **2**, 1079 (2013).
[34]C. Liu, S. Hu, and S. Shen, Smart Mater. Struct. **21**, 115024 (2012).
[35]Y. Xu, S. Hu, and S. Shen, Comput. Modell. Eng. Sci. **91**, 397 (2013).
[36]H. Allik and T. J. R. Hughes, Int. J. Numer. Methods Eng. **2**, 151 (1970).
[37]B. T. Darrall, A. R. Hadjesfandiari, and G. F. Dargush, Eur. J. Mech. A-Solids **49**, 308 (2015).
[38]Y. Gao and Z. L. Wang, Nano Lett. **9**, 1103 (2009).
[39]X. Liang, S. Hu, and S. Shen, Smart Mater. Struct. **24**, 105012 (2015).
[40]P. V. Yudin and A. K. Tagantsev, Nanotechnology **24**, 432001 (2013).
[41]A. Safari and E. K. Akdogan, *Piezoelectric and Acoustic Materials for Transducer Applications* (Springer US, 2008).
[42]Y. Gao and Z. L. Wang, Nano Lett. **7**, 2499 (2007).
[43]C. L. Sun, J. A. Shi, and X. D. Wang, J. Appl. Phys. **108**, 034309 (2010).
[44]H. Grimmer, Acta Crystallogr., Sect. A: Found. Crystallogr. **63**, 441 (2007).
[45]P.-Y. Prodhomme, A. Beya-Wakata, and G. Bester, Phys. Rev. B **88**, 121304 (2013).
[46]See supplementary material at http://dx.doi.org/10.1063/1.4946843 for details of fully coupled FEA method, the linear piezoelectric coefficient matrix, the complete expansion of the strain gradient, the direct flexoelectric coefficient matrix, material constants used in calculation, supportive calculation of nonlinear piezoelectric potential distribution along a ZnO NW, piezoelectric and flexoelectric potential distributions along a ZnO NW, and comparison of piezoelectric potential distribution along a BTO NW calculated by the two methods.